Supporting Information for "Mediterranean Tropical-Like Cyclones forecasts and analysis using the ECMWF Ensemble Forecasting System (IFS) with Physical Parameterizations Perturbations"

Miriam Saraceni[1], Lorenzo Silvestri[2], Peter Bechtold[3], and Paolina Bongioannini Cerlini[4]

[1,2]Department of Civil and Environmental Engineering, University of Perugia, Perugia, Italy
[4]Department of Physics and Geology, University of Perugia, Perugia, Italy
[3]European Centre for Medium-Range Weather Forecasts, Bonn, Germany

Correspondence: Miriam Saraceni (miriam.saraceni@unipg.it)

In this supporting information, we provide a deep explanation of all the perturbed parameters of the Stochastically Perturbed Parameterization (SPP) in Section S1 and a brief description of some of the statistical scores used in this study (Section S2). Then, some additional Figures are reported. In **Figure S1** we provide the ensemble standard deviation for each experiment for the daily accumulated precipitation for the corresponding dates in the main text to give a complete analysis and show where there is more uncertainty in the ensemble forecast simulation. In **Figure S2** the Root Mean Squared Error (RMSE) is provided as it changes for increasing starting date for the daily maximum precipitation, in order to assess how it is decreasing with increasing starting dates at least for Ianos and Zorbas.

Figure S3 and **Figure S4** represent the presence of a deep upper tropospheric trough, cut off from the large-scale circulation and intruding into the Mediterranean area, in the operational analysis and in the ensemble simulations. In these Figures, the 500 hPa Geopotential Height (m), temperature (K), and wind (m/s) are reported in relation to the mean sea level pressure field (hPa). The Figures show that While for Ianos and Zorbas, the presence of the cut-off low is well simulated by the ensemble experiments (Figure SS4a to d), the occurrence of the double cut-off in Trixie is accompanied, in ensemble simulations, by the disappearance of the low that sustained the cyclone, as it is shown in Figure SS4e and f. If one looks at the tracking, all the tracks follow the second cut-off low, because the first one is too weak and disappears before the 29th. This is also linked to the fact that Trixie is not able to be sustained after the 28th-29th in the ensembles and it is not going through the tropical-like phase as in the analysis. This behavior, which is presented here for the simulation starting on the 26th, is consistent also for the other starting dates, with the first cut-off low decreasing intensity and almost disappearing for earlier starting dates. This is reported in **Figure S5**. Indeed **Figure S5** shows the change with increasing starting dates in the deep cut-off low simulation in both the SPP-Conv and the INI experiment to underline the difference within the change of initial conditions.

In **Figure S6** the change in the Potential Vorticity isosurfaces at 2 PVU in the SPP-Conv experiment by increasing starting dates is shown to capture the evolution of the forecast with a better reproduction of the alignment between the upper-level disturbance of the PV field and the heating at 500 hPa. Lastly in **Figure S7** the Total Heat Flux, the sum of the latent heat flux and the sensible heat flux, is shown for each ensemble mean belonging to each experiment, the SPP-Conv, the INI and the SPP

ensembles, for the time-step in which the cyclone is entering in its tropical-like phase. This is done to underline the different
25   contributions of surface fluxes in the three medicanes.

S1   Perturbed parameters

The implementation of SPP allows simultaneous perturbations of up to 27 parameters and variables in the deterministic IFS parametrizations. These 27 parameters and variables are reported in Tables S1 - S4.

30   S1.1   Turbulent diffusion and Boundary layer processes

Regarding the boundary layer processes, one of the most important aspects is the turbulent transfer, with which the atmospheric model knows about the surface boundary condition. Land surfaces tend to be heterogeneous and it is challenging to characterize real terrain in terms of the surface drag that it exerts on the flow, especially in areas with orography. Usually, the Monin Obukhov Similarity is used, which applies to stationary homogeneous conditions. Furthermore, there is much un-
35   certainty regarding the interaction between turbulence and ocean waves. Given that the atmospheric circulation is sensitive to surface drag (Sandu et al., 2016), the chosen parameters of the scheme to be perturbed are related to the surface drag and the sub-grid orography scheme. Furthermore, the von Kármán constant is perturbed, because several uncertain quantities in the turbulent diffusion scheme are proportional to the von Kármán constant. These are the standard deviation of vertical velocity, which is estimated via an empirical formula, the Obukhov length used to compute the stability functions in the outer layer for
40   surface-driven diffusion, the surface-layer (the level below the lowest model level) mixing length used in the outer layer (the level above the lowest model level) and the cloud-top driven diffusion. It has to be underlined here that the perturbation to the transfer coefficient for momentum over land and over the ocean and the von Kármán constant is changed to be dependent on the type of planetary boundary layer (PBL) type.

45   S1.2   Convection

Regarding the convective parameterization, the most uncertain processes are the mixing of the cloud with the environment (detrainment and entrainment rates) and the mixing in the sub-cloud layer, the autoconversion in the microphysics of clouds, and the convective momentum transport. The uncertainty of the latter is of particular interest because it depends on the organization of convection and on the fact that it usually acts to reduce the shear, while in the mesoscale convective system, it can also have
50   an opposite effect (Ollinaho et al., 2017). Indeed, the perturbation regards the zonal and meridional convective momentum transport due to shallow and deep convection.

Table S1. Perturbed parameter settings for the turbulent diffusion and subgrid orography parameterization. The first column is the parameter identifier, the second is a brief explanation of the role of the parameter in the model. The third column (dist.) indicates the sampled distribution type: LN and N refer to the log-normal and normal distribution, respectively. The fourth column presents the standard deviations of the two underlying Gaussian distributions.

Parameter ID	Role of the parameter	Dist	σ	Scheme
CFM_{OC}	Transfer coefficient for momentum over ocean	LN	0.26, for dry convective PBL 0.33	Mean/Median
CFM_{LA}	Transfer coefficient for momentum over land	LN	0.65, for dry convective PBL 0.78	Mean/Median
$RKAP$	von Kármán constant	LN	0.65, for dry convective PBL 0.26	Mean/Median
$TOFDC$	Coefficient in turbulent orographic form drag scheme	LN	0.78	Mean
$HSDT$	St. dev. of subgrid orography	LN	0.52	Mean
$VDEXC_{LEN}$	Length-scale for vertical mixing in stable boundary layer	LN	1.04	Mean

S1.3 Clouds and large scale precipitation processes

Concerning the parameterization of clouds and precipitation microphysics, perturbation is added to the different processes of
55 cloud formation, cloud dissipation, rain formation, and snow aggregation. The rain evaporation rate, the snow sublimation rate, and the vertical velocity that is used to calculate the adiabatic temperature change for saturation adjustment of condensation and evaporation are perturbed. These perturbations are chosen as they directly change latent heating, which affects atmospheric stability and tropospheric dynamics, particularly in the storm tracks (Attinger et al., 2019, 2021). Indeed, these processes' uncertainty comes from the low understanding of the rain and snow particle size distributions, terminal fall speeds, and particle
60 properties (Boutle and Abel, 2012). Other uncertainties come from the variability of adiabatic heating and cooling, which drives condensation and evaporation. Other perturbations regard the critical relative humidity parameter characterizing the sub-grid heterogeneity of humidity in a grid box and define the relative humidity at which condensation begins to form in the respective grid box.

S1.4 Radiation

65

Finally, regarding radiation parameterization, the greatest source of uncertainty in the IFS radiation scheme is the treatment of clouds and aerosols (Morcrette et al., 2008). Indeed, with the use of the Monte Carlo Independent Column Approximation (McICA) to represent sub-grid cloud distribution from the cloud fraction and grid box mean cloud water content, uncertainty

Table S2. Perturbed parameter settings for the convection parameterization. The first column is the parameter identifier, the second is a brief explanation of the role of the parameter in the model. The third column (dist.) indicates the sampled distribution type: LN and N refer to the log-normal and normal distribution, respectively. The fourth column presents the standard deviations of the two underlying Gaussian distributions.

Parameter ID	Role of the parameter	Dist	σ	Scheme
$ENTRORG$	Entrainment rate	LN	0.39	Mean
$ENTSHALP$	Shallow entrainment rate	LN	0.39	Mean
$DETRPEN$	Detrainment rate for penetrative convection	LN	0.39	Mean
$RPRCON$	Conversion coefficient cloud to rain	LN	0.52	Mean
$CUDU$	Zonal convective momentum transport, deep convection	N	1.22	Mean
$CUDV$	Meridional convective momentum transport, deep convection	N	1.22	Mean
$CUDUS$	Zonal convective momentum transport, shallow convection	N	1.33	Mean
$CUDVS$	Meridional convective momentum transport, shallow convection	N	1.33	Mean
$RTAU$	Adjustment time-scale in CAPE closure	LN	0.78	Mean
$ENTSTPC1$	Shallow entrainment test parcel entrainment	LN	0.39	Mean

may arise due to the vertical decorrelation length scale governing the degree to which clouds in adjacent layers overlap, and
70 due to the fractional standard deviation of water content in a given model layer. regarding aerosols, their optical depth for 5 different species is prescribed from a climatology derived from (Tegen et al., 1997). The climatology varies as a function of longitude, latitude, and month. To compute the 3D aerosol distribution, concentrations are assumed to decrease exponentially with height according to a specified scale height for each species. SPP perturbs aerosol optical depth and this scale height independently. Moreover, the other important aspect of parameterization is converting water content to the optical depth of a
75 layer. This is done by parameterizing it as a function of effective radius, which for liquid clouds is calculated as a function of liquid water content (Martin et al., 1994), while ice is a function of temperature. Both parameters are perturbed.

S2 Verification scores

Wilks (2011) provide extensive details on many verification scores, as well as the ECMWF web page (https://confluence.
80 ecmwf.int/x/4fbUBw) on statistical concepts and probabilistic data. The verification procedure involves a comparison between

Table S3. Perturbed parameter settings for the cloud and large-scale precipitation parameterization. The first column is the parameter identifier, the second is a brief explanation of the role of the parameter in the model. The third column (dist.) indicates the sampled distribution type: LN and N refer to the log-normal distribution and the normal distribution, respectively. The fourth column presents the standard deviations of the two underlying Gaussian distributions.

Parameter ID	Role of the parameter	Dist	σ	Scheme
$RAMID$	Relative humidity threshold for the onset of stratiform condensation	LN	0.13	Mean
$RCLDIFF$	Diffusion coefficient for the evaporation of cloud at subgrid cloud edges	LN	1.04	Mean
$RLCRITSNOW$	Cloud ice threshold for autoconversion to snow	LN	0.78	Mean
$RAINEVAP$	Rain evaporation rate	LN	0.65	Mean
$SNOWSUBLIM$	Snow sublimation rate	LN	0.65	Mean
$QSATVERVE$	Vertical velocity used to calculate the adiabatic temperature change for saturation adjustment	LN	0.39	Mean

Table S4. Perturbed parameter settings for the radiation parameterization. The first column is the parameter identifier, the second is a brief explanation of the role of the parameter in the model. The third column (dist.) indicates the sampled distribution type: LN and N refer to the log-normal and normal distribution, respectively. The fourth column presents the standard deviations of the two underlying Gaussian distributions.

Parameter ID	Role of the parameter	Dist	σ	Scheme
$ZDECORR$	Cloud vertical decorrelation height	LN	0.78	Mean
$ZSIGQCW$	Fractional st. dev. of horiz. distribution of water content	LN	0.52	Mean
$ZRADEFF$	Effective radius of cloud water and ice	LN	0.78	Mean
ZHS_{VDAERO}	Scale height of aerosol normal vertical distribution	LN	1.04	Mean
$DELTA_{AERO}$	Optical thickness of aerosol	LN	0.78	Mean

matched pairs of forecasts and the observations to which they pertain. In the following, the verification scores used in the manuscript are described.

S2.1 Relative Operating Curve

The Receiver Operating Characteristic (ROC) is a measurement of the forecast's ability to distinguish between two alternative outcomes and thus, measures resolution. The ROC was first introduced to meteorology by Mason in 1982 and is obtained by plotting the probability of detection (POD) against the probability of false detection (POFD) using a set of increasing probability thresholds. The ROC area, which is the area under the ROC curve, is often used as a score. A score of 0.5 indicates no skill and a score of 1 indicates perfect skill. It's important to note that ROC can also be computed for deterministic forecasts using different criteria such as median, certain percentiles, or chosen thresholds of interest instead of the probability thresholds used in probabilistic forecasts.

S2.2 Brier score

The Brier score (Brier et al., 1950), introduced by Brier in 1950, is a measure of the accuracy of probability forecasts in terms of predicting whether or not an event occurred. It is defined as the mean squared error of probabilistic forecasts, with events assigned a value of 1 and non-events assigned a value of zero. It has a mathematical structure similar to the Mean Square Error (MSE).

$$BS = \overline{(p - o)^2} \tag{1}$$

Thus, BS measures the difference between the forecast probability of an event (p), and its occurrence (o). The Brier score ranges from 0 to 1 with a perfect score of 0. Indeed it is a measure of the mean squared probability error of a forecast compared to a reference dataset such as observations, analyses, or climatology. The Brier Score for the forecast is calculated as the mean squared probability error of the forecast against observations or analyses over a given period. A lower Brier Score indicates a more accurate forecast, with a score of 0 indicating a wholly accurate forecast and a score of 1 indicating a wholly inaccurate forecast.

S3 Figures
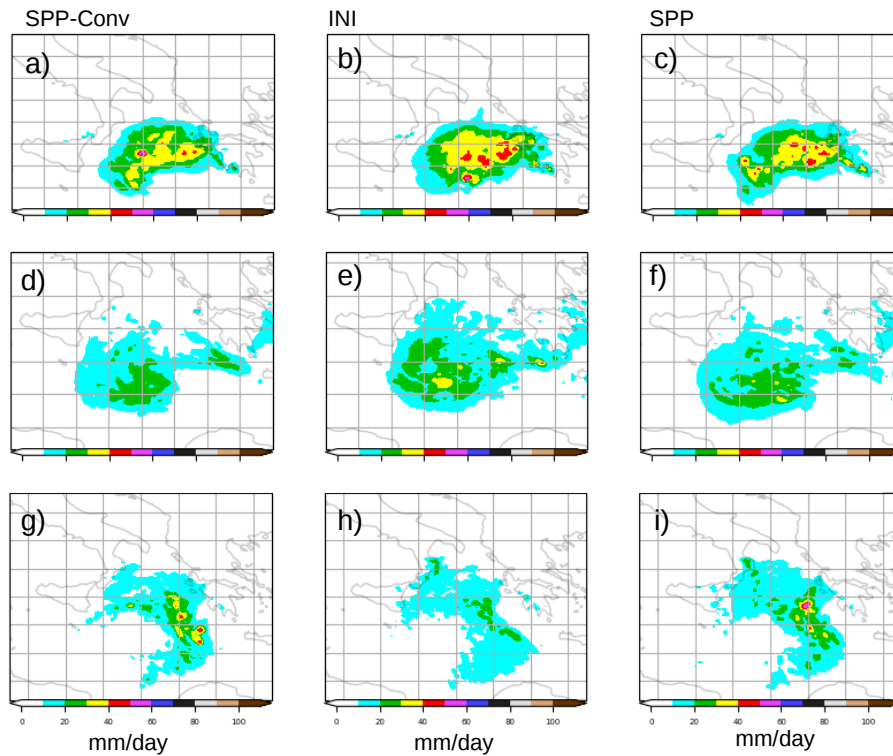
Figure S1. Daily accumulated precipitation (mm/day) standard deviation for the three ensemble experiments ensemble means. For Ianos the 17th is shown in Figures (a), (b) and (c). For Zorbas the 28th is shown in Figures (d), (e) and (f). For Trixie the 28th is shown in Figures (g), (h) and (i). the SPP-Conv ensemble forecast ensemble mean accumulated precipitation standard deviation is reported in the first column, the SPP ensemble mean in the second column and the INI ensemble mean in the third column. For Ianos the experiments starting on the 17th are shown, for Zorbas the ones starting on the 27th and for Trixie the ones starting from the 27th
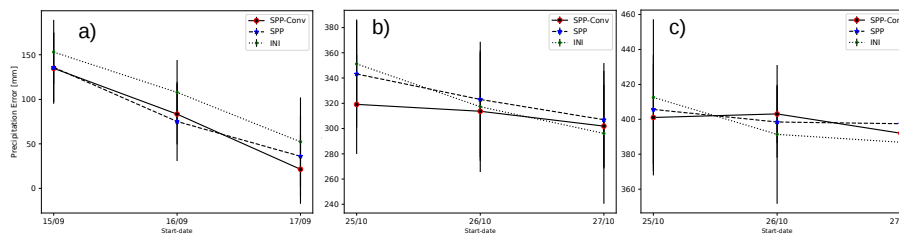
Figure S2. Daily accumulated precipitation (mm/day) root mean squared error between the ensemble mean maximum precipitation and the observed maximum precipitation evolution with increasing starting date for the three ensemble experiments ensemble means. For Ianos in Figure (a) the 17th maximum precipitation is taken, for Zorbas in Figure (b) the 28th maximum precipitation is taken and for Trixie in Figure (c) the 28th maximum precipitation is taken.
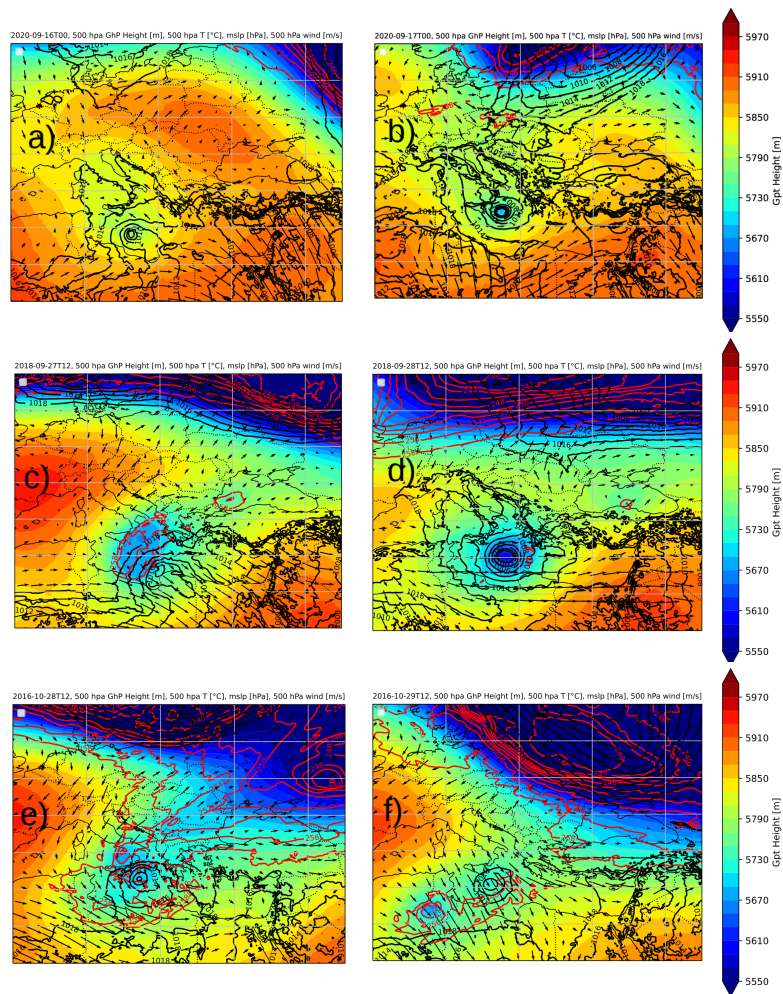
Figure S3. 500 hPa Geopotential height, together with the 500 hPa temperature (red lines) and mean sea level pressure (black lines) for the three medicanes as reproduced by the operational analysis. Ianos synoptic situation is shown for the 16th at 00 UTC in Figure (a) and for the 17th at 00 UTC in Figure (b). Zorbas synoptic situation is shown for the 27th at 12 UTC in Figure (c) and for the 28th at 12 UTC in Figure (d). Trixie synoptic situation is shown for the 28th at 12 UTC in Figure (e) and for the 29th at 12 UTC in Figure (f)
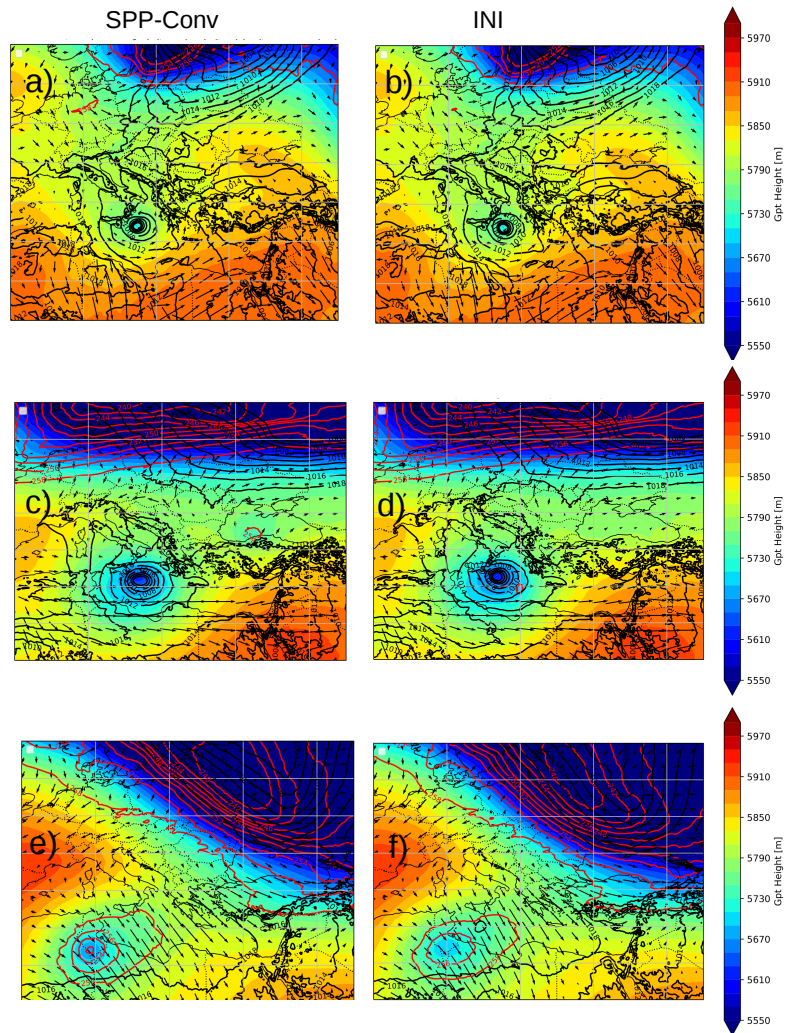
Figure S4. 500 hPa Geopotential height, together with the 500 hPa temperature and mean sea level pressure for the three medicanes as reproduced by the SPP-Conv ensemble in the first column and the INI ensemble in the second column. Ianos synoptic situation is shown for the 17th at 00 UTC in Figures (a) and (b). Zorbas synoptic situation is shown for the 28th at 12 UTC in Figures (c) and (d). Trixie synoptic situation is shown for the 29th at 12 UTC in Figures (e) and (f).
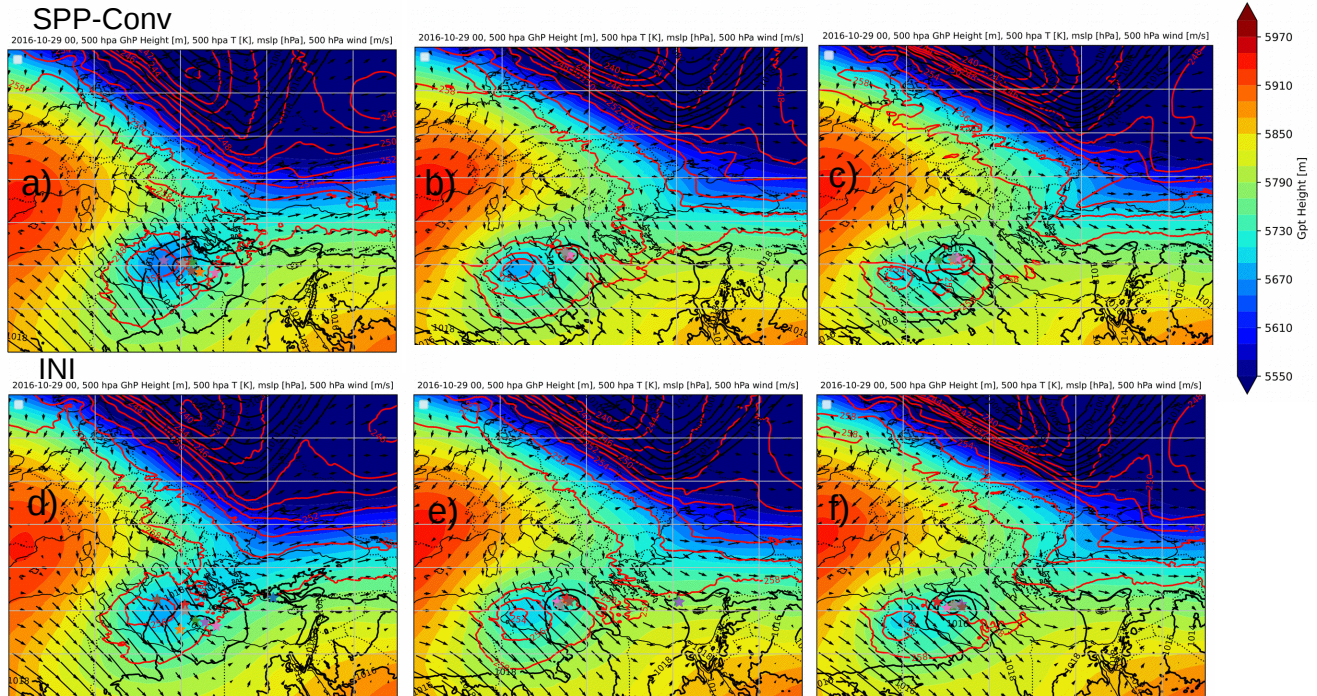
Figure S5. 500 hPa Geopotential height together with the 500 hPa temperature (red lines), mean sea level pressure (black lines), and central position of the ensemble members cyclones (stars) for Trixie cyclones. The 29th at 00 UTC is shown as simulated by the SPP-Conv ensemble for increasing starting dates from the 25th to the 27th in Figures (a), (b) and (c) respectively. The INI ensemble is reported for increasing starting date in Figures (d), (e) and (f) for comparison.
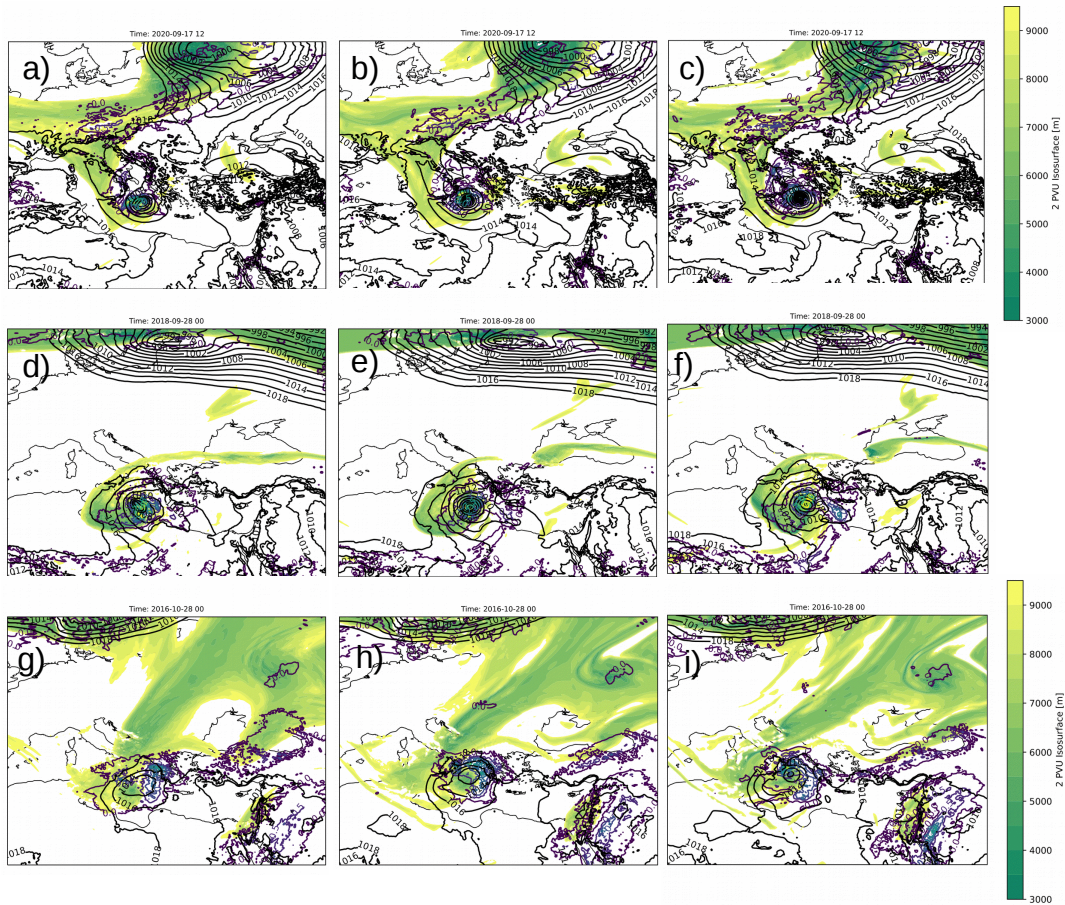
Figure S6. Height of the 2 PVU (PVU = $m^2 K kg^{-1} s^{-1} 10^{-6}$) isosurfaces together with the mean sea level pressure (black lines) and Q1 at 500 hPa for the SPP-Conv ensemble experiment ensemble mean with the increasing starting date. For Ianos the 17th at 12 UTC is reported in Figure (a) as simulated by the experiment starting from the 15th, in (b) as simulated by the experiment starting from the 16th and in (c) as simulated by the experiment starting from the 17th. For Zorbas the 28th at 00 UTC is reported in Figure (d) as simulated by the experiment starting from the 25th, in (e) as simulated by the experiment starting from the 26th and in (f) as simulated by the experiment starting from the 27th. For Trixie the 28th at 00 UTC is reported in Figure (g) as simulated by the experiment starting from the 25th, in (h) as simulated by the experiment starting from the 26th and in (i) as simulated by the experiment starting from the 27th .
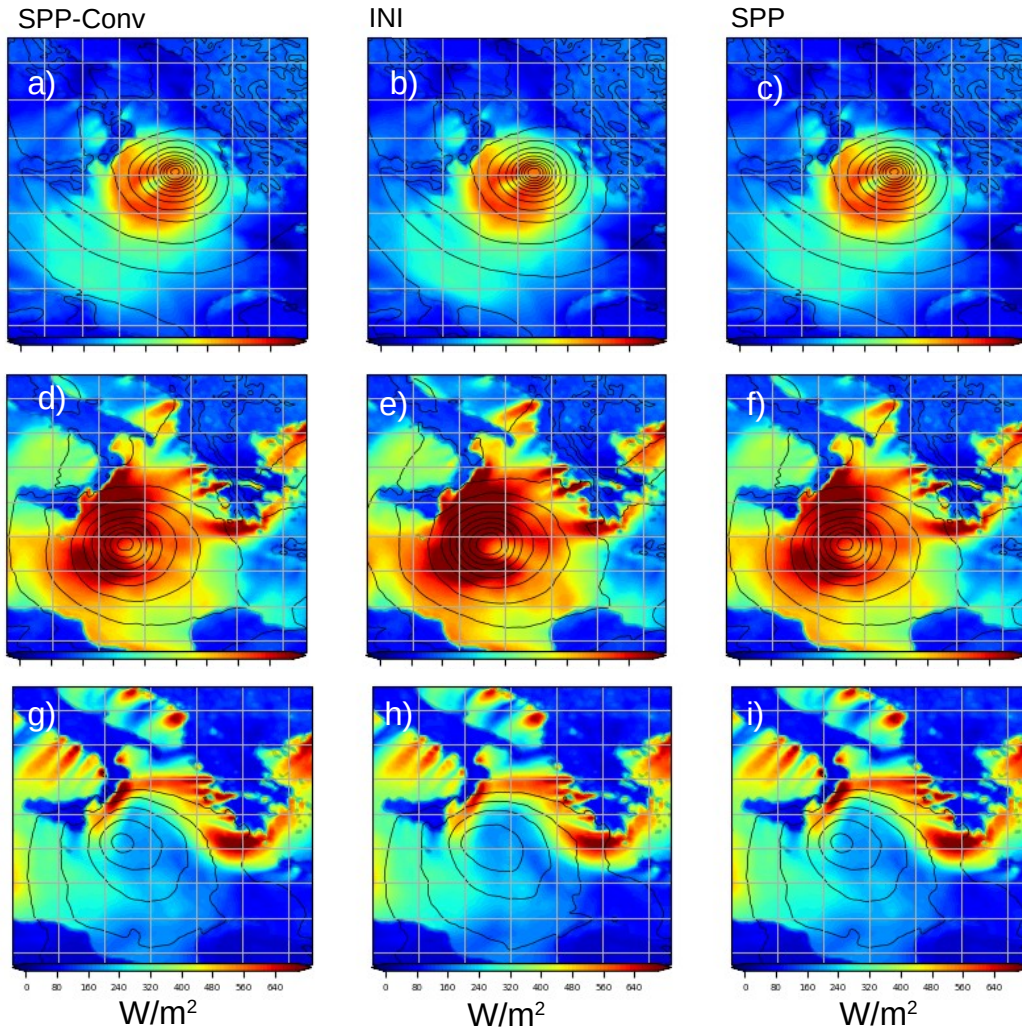
Figure S7. Total surface fluxes (sum of the latent heat flux and the sensible heat flux) (W/m^2) for the three ensemble experiments ensemble means. For Ianos the 17th at 12 UTC is shown in Figures (a), (b) and (c). For Zorbas the 28th at 12 UTC is shown in Figures (d), (e) and (f). For Trixie the 28th at 12 UTC is shown in Figures (g), (h) and (i). the SPP-Conv ensemble forecast ensemble mean is reported in the first column, the SPP ensemble mean in the second column and the INI ensemble mean in the third column. For Ianos the experiments starting on the 17th are shown, for Zorbas the ones starting on the 27th and for Trixie the ones starting from the 27th

References

Attinger, R., Spreitzer, E., Boettcher, M., Forbes, R., Wernli, H., and Joos, H.: Quantifying the role of individual diabatic processes for the formation of PV anomalies in a North Pacific cyclone, Quarterly Journal of the Royal Meteorological Society, 145, 2454–2476, 2019.

Attinger, R., Spreitzer, E., Boettcher, M., Wernli, H., and Joos, H.: Systematic assessment of the diabatic processes that modify low-level potential vorticity in extratropical cyclones, Weather and Climate Dynamics, 2, 1073–1091, 2021.

Boutle, I. and Abel, S.: Microphysical controls on the stratocumulus topped boundary-layer structure during VOCALS-REx, Atmospheric Chemistry and Physics, 12, 2849–2863, 2012.

Brier, G. W. et al.: Verification of forecasts expressed in terms of probability, Monthly weather review, 78, 1–3, 1950.

Martin, G., Johnson, D., and Spice, A.: The measurement and parameterization of effective radius of droplets in warm stratocumulus clouds, Journal of Atmospheric Sciences, 51, 1823–1842, 1994.

Morcrette, J., Barker, H. W., Cole, J., Iacono, M. J., and Pincus, R.: Impact of a new radiation package, McRad, in the ECMWF Integrated Forecasting System, Monthly weather review, 136, 4773–4798, 2008.

Ollinaho, P., Lock, S.-J., Leutbecher, M., Bechtold, P., Beljaars, A., Bozzo, A., Forbes, R. M., Haiden, T., Hogan, R. J., and Sandu, I.: Towards process-level representation of model uncertainties: stochastically perturbed parametrizations in the ECMWF ensemble, Quarterly Journal of the Royal Meteorological Society, 143, 408–422, 2017.

Sandu, I., Bechtold, P., Beljaars, A., Bozzo, A., Pithan, F., Shepherd, T. G., and Zadra, A.: Impacts of parameterized orographic drag on the N orthern H emisphere winter circulation, Journal of Advances in Modeling Earth Systems, 8, 196–211, 2016.

Tegen, I., Hollrig, P., Chin, M., Fung, I., Jacob, D., and Penner, J.: Contribution of different aerosol species to the global aerosol extinction optical thickness: Estimates from model results, Journal of Geophysical Research: Atmospheres, 102, 23 895–23 915, 1997.

Wilks, D. S.: Statistical methods in the atmospheric sciences, vol. 100, Academic press, 2011.